Coherent precipitation and stability of cuboidal B2 nanoparticles in a ferritic Fe–Cr–Ni–Al superalloy

Zhenhua Wang, Qing Wang, Ben Niu, Chuang Dong, Hongwei Zhang, Haifeng Zhang & Peter K. Liaw

MATERIALS RESEARCH LETTERS

Taylor & Francis
Taylor & Francis Group

ORIGINAL REPORT

∂ OPEN ACCESS   Check for updates

Coherent precipitation and stability of cuboidal B2 nanoparticles in a ferritic Fe–Cr–Ni–Al superalloy

Zhenhua Wang[a], Qing Wang[a], Ben Niu[a], Chuang Dong[a], Hongwei Zhang[b], Haifeng Zhang[b] and Peter K. Liaw[c]

[a]Key Laboratory of Materials Modification by Laser, Ion and Electron Beams (Ministry of Education), Engineering Research Center of High Entropy Alloy Materials (Liaoning Province), School of Materials Science and Engineering, Dalian University of Technology, Dalian, People's Republic of China; [b]Shenyang National Laboratory for Materials Science, Institute of Metal Research, Chinese Academy of Sciences, Shenyang, People's Republic of China; [c]Department of Materials Science and Engineering, The University of Tennessee, Knoxville, TN, USA

ABSTRACT

The present work developed a new Fe-based superalloy of Fe–10.9Cr–13.9Ni–6.4Al–2.2Mo–0.5W–0.04Zr–0.005B (weight percent, wt. %) with cuboidal B2 nanoparticles coherently precipitated into the body-centred-cubic (BCC) matrix. This alloy possesses excellent microstructural stability at 973 K with a slow particle coarsening rate and the B2 nanoprecipitates still keep cuboidal after 1000 h-aging, which is ascribed to the moderate lattice misfit ($\epsilon = 0.24$–0.67%) between BCC and B2 phases. Also, the current alloy exhibits a prominent mechanical property with a high yield strength of $\sigma_{YS} = 238$–258 MPa at 973 K.

IMPACT STATEMENT

A Fe-based superalloy with cuboidal B2 nanoparticles coherently precipitated into BCC matrix exhibits high microstructural stability and prominent mechanical property at 973 K.

Introduction

Fe-based superalloys (or heat-resistant ferritic stainless steels, FSSs) have been widely applied into high-temperature (HT) fields due to their prominent mechanical property, high thermal conductivity, and low thermal expansion [1–4]. They are generally strengthened by carbides ($Cr_{23}C_6$ and MC, M = Nb, Ti, V, etc.), Laves phase (Fe_2M), and Z-CrNbN [1–5]. However, the creep resistance of these alloys would degrade after a long-term operation at HTs (above 923 K) due to the microstructural instability, i.e. the rapid coarsening of precipitates induced by the non-coherency with the body-centred-cubic (BCC) ferritic matrix [3,4]. Considering that the superiority of Ni-based superalloys at HTs (> 1073 K) benefits from their unique microstructure of spherical or cuboidal γ'-Ni_3Al ordered nanoparticles coherently precipitated in face-centred-cubic (FCC)-γ matrix [6–8], the coherent precipitation of ordered B2 nanoparticles in the BCC matrix would undoubtedly improve the HT microstructural stability and mechanical properties of Fe-based superalloys. It is demonstrated that in the Fe–10Cr–10Ni–6.5Al–3.4Mo–0.25Zr–0.005B

(weight percent, wt. %, designated as FBB8) alloy, the coherent precipitation of spherical B2-NiAl nanoparticles in BCC ferritic matrix indeed exhibits higher microstructural stability than the non-coherent precipitation in traditional FSSs at 973 K [9,10]. Intriguingly, the further addition of 2 wt. % Ti into FBB8 could produce cuboidal B2-NiAl/$L2_1$-Ni_2AlTi hierarchical nanoprecipitates, in which the $L2_1$-Ni_2AlTi is another highly ordered phase of BCC solid solution [11–13]. This significantly enhances the tensile yield strength from original 120 MPa up to 280 MPa at 973 K due to the cuboidal nanoprecipitation, which is also much higher than that (160 MPa at 923 K) of Fe–13Cr–4.5Al–2Mo–1Nb (wt. %) FSS strengthened by $Fe_2(Mo,Nb)$ Laves phase [13,14]. It is known that the formation of spherical or cuboidal nanoprecipitates is closely related to the lattice misfit ϵ between BCC and B2 phases [15–18], in which the particle morphology would change from spherical to cuboidal, and to rod- or needle shape with increasing the ϵ. And only a moderate ϵ could result in a coherent microstructure with cuboidal B2 nanoprecipitates, as evidenced by the fact that the relatively larger $\epsilon = 0.7\%$ and the smaller $\epsilon = 0.06\%$

correspond to the formation cuboidal B2/L2$_1$ and spherical B2 nanoprecipitates in FBB8 alloys with and without Ti, respectively [9–11]. Unfortunately, the addition of Ti would deteriorate the resistance to oxidation since Ti accelerates the internal oxidation due to its relatively high oxygen permeability at HTs [19]. Therefore, to develop novel Fe-based superalloys or FSSs strengthened by cuboidal B2-NiAl precipitates would be fascinating for HT structural applications.

It is difficult to tailor the BCC/B2 lattice misfit to a moderate value moderately for cuboidal nanoprecipitation since there exists a relatively larger composition difference between them, which is different from that in Ni-based superalloys [6–8]. Generally, a large composition difference between BCC/B2 would result in a large lattice misfit to form a typical weave-like microstructure [20,21]. So it is challenging to develop the Fe-based superalloys with cuboidal B2 nanoprecipitates in BCC ferritic matrix due to a much larger composition difference between them, in which the BCC/B2 would like to exhibit a weave-like microstructure [20,21]. In previous works, we have developed a series of multi-component alloys with cuboidal B2 nanoprecipitates in the BCC matrix using in light of the cluster composition formula of Al$_2$M$_{14}$ (M represents different combinations of Fe, Co, Ni, and Cr), which exhibit high microstructural stability at HTs and prominent mechanical properties showing a coherent microstructure with cuboidal B2 nanoprecipitates in the BCC matrix [15–17]. Here, by setting the M as M$_{14}$ = Fe$_{10}$Ni$_2$Cr$_2$, we can obtain the composition of Al$_2$(Fe$_{10}$Ni$_2$Cr$_2$) (= Fe–12.5Cr–14.1Ni–6.5Al, wt. %), which is a Fe-based superalloy according to the Cr- and Ni-equivalence in stainless steels [22]. In addition, the addition of Mo could increase the lattice constant of BCC matrix, leading to a favourable reduction in the BCC/B2 lattice misfit [23,24]. As slow diffusing elements, both Mo and W could inhibit the coarsening of B2 particles since they would like to segregate on the BCC/B2 interfaces [10]. Thus a minor amount of Mo and W is substituted for Cr in the above composition with a specific ratio of Cr to (Mo + W) = 8/1 (in molar fraction). A trace amount of Zr and B should also be added to improve the ductility of high-strength steels through enhancing grain-boundary cohesion for the prevention of intergranular fracture [25,26]. Therefore, the optimal composition is finally determined as Fe–10.9Cr–13.9Ni–6.4Al–2.2Mo–0.5W–0.04Zr–0.005B (wt. %) to achieve the BCC/B2 coherent microstructure with cuboidal B2 nanoprecipitates. Then, the BCC/B2 microstructural evolution with the aging time at 973 K will be investigated, in which the coarsening behaviour of cuboidal B2 nanoparticles will be discussed. Moreover, the mechanical property of this alloy at both room temperature and 973 K will be studied, where the strengthening mechanisms are also elucidated.

Experimental

The current alloy ingots were prepared by arc melting and suction cast into a 6-mm-diameter cylindrical copper mould under an argon atmosphere. The purities of raw metals are 99.999 wt. % for Al, 99.99 wt. % for Fe, Ni, Zr, and B, and 99.9 wt. % for Cr, Mo, and W, respectively. These ingots were remelted at least five times to ensure composition uniformity. Both cast ingots and rods were solid-solutionized (ST) at 1473 K for 2 h in a muffle furnace. Then, these ST specimens were aged at 973 K for different times up to 1000 h. Each heat treatment was followed by water quenching. The crystalline structures of alloy specimens at different treatments were identified, using a Bruker D8 X-ray diffractometer (XRD) with the Cu K_α radiation (λ = 0.15406 nm). The microstructure was examined using Olympus optical microscopy (OM), Zeiss Supra 55 scanning electron microscopy (SEM), and JEM2100F FEG scanning transmission electron microscopy (STEM). The etching solution for OM and SEM observation was composed of 5 g FeCl$_3$·6H$_2$O + 25 ml HCl + 25 ml C$_2$H$_5$OH, and the TEM specimens were prepared by twin-jet electron-polishing in a solution of 10% HClO$_4$ + 90% C$_2$H$_5$OH (volume fraction) at a cryogenic temperature of 243 K. Elemental distribution of the aged alloy was analysed, using an FEI Helios NanaLab 600 Dual-Beam focused ion beam (DB-FIB) instrument equipped with the energy-dispersive spectrometer (EDS). The chemical composition was analysed using SHIMADZU electronic probe micro-analyser (EPMA) with a Super-X energy dispersive. The melting temperature of this alloy was measured by NETZSCH STA 449F3 Differential Scanning Calorimetry (DSC) with a heating rate of 10 K/min. The statistical analysis of the volume fraction and size of precipitated particles and the grain sizes at different heat-treated states were measured from the SEM/OM morphology images (at least 6 images) employing the ImageJ software [27]. The mean radius (r) of precipitates is calculated from the traced areas using a circular-equivalent, i.e. $r = \sqrt{(\text{area}/\pi)}$. Microhardness of different heat-treated samples was tested with an HVS-1000 Vickers hardness tester under a load of 500 g for 15 s, in which at least 10 indents were taken to obtain an average value. Uniaxial tensile tests at 973 K were conducted on a UTM5504 Material Test System (MTS) with a heating furnace and with a nominal strain rate of 1×10^{-3} s^{-1}. The gauge dimension of tensile samples is 3 mm in diameter and 25 mm in

length, and three samples for each heat treatment were tested.

Results and discussion

The chemical composition of the current solid-solutionized alloy with the EPMA analysis is Fe–(11.08 ± 0.15)Cr–(11.85 ± 0.08)Ni–(5.90 ± 0.08)Al–(2.19 ± 0.02)Mo–(0.51 ± 0.03)W–(0.04 ± 0.02)Zr–(0.004 ± 0.003)B (wt. %), which is close to the nominal composition.

And the melting temperature of this alloy measured by DSC is about 1679 K (Figure S1, in Supplementary Material), which is comparable to those (1671–1727 K) of existing commercial stainless steels containing a certain amount of Cr and Ni [28]. The XRD results in Figure S2 show that all the alloy specimens in different heat-treated states consist of primary BCC solid solution plus a B2 phase (characterized by a weak (100) diffraction peak). The lattice constants of these two phases were then calculated, being $a_{BCC} = 0.2877 \pm 0.0042$ nm and
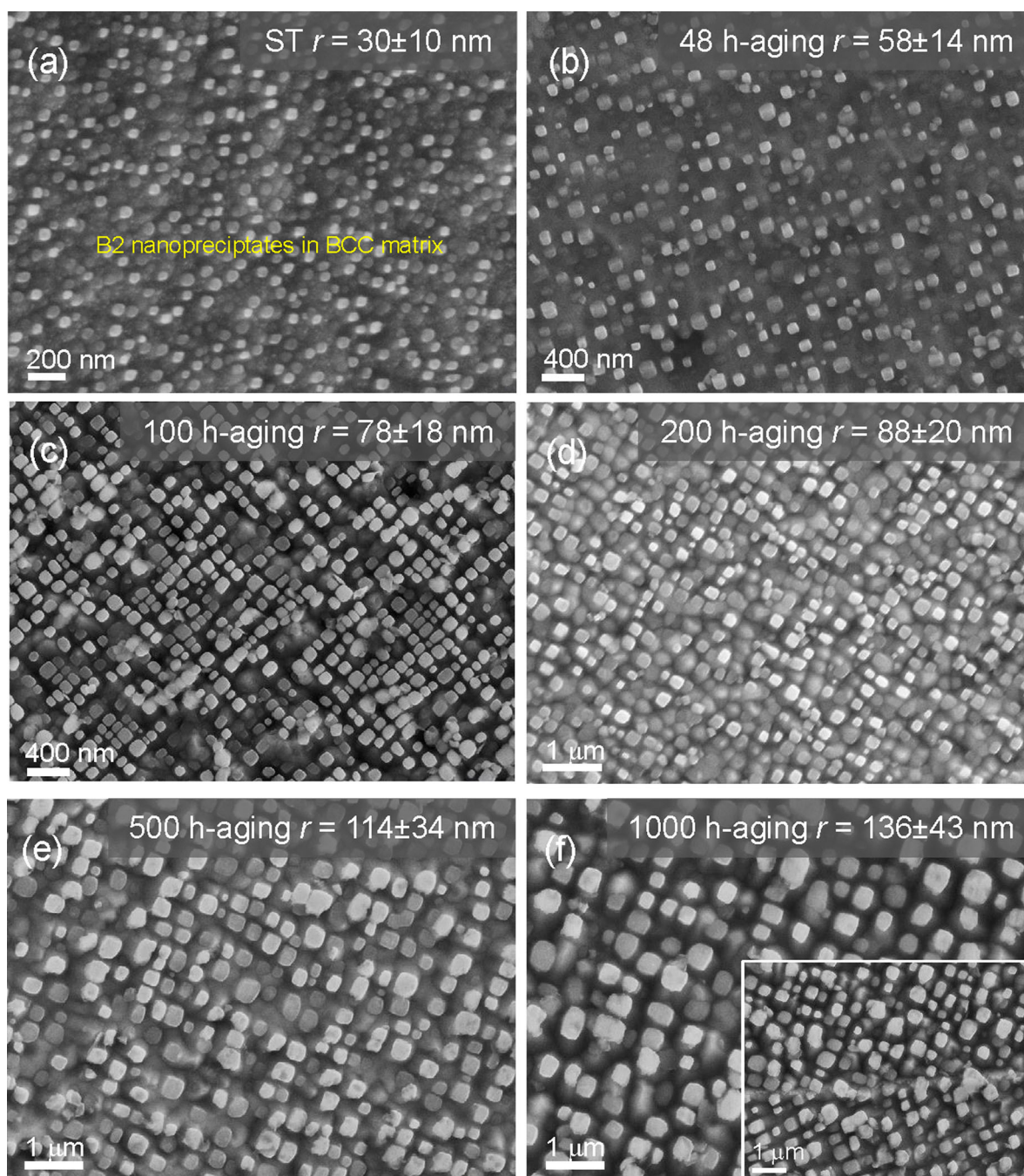

Figure 1. SEM observations of the current alloy after different heat treatments: (a) solid-solutionized at 1473 K for 2 h, (b–f) aged at 973 K for 48 h, 100 h, 200 h, 500 h, and 1000 h, respectively.

$a_{B2} = 0.2887 \pm 0.0047$ nm, respectively. Moreover, the lattice misfit calculated with the equation of $\epsilon = 2 \times (a_{B2} - a_{BCC})/(a_{B2} + a_{BCC})$ [29] could increase from $\epsilon = 0.24\%$ in 0.5 h-aged sample to $\epsilon = 0.67\%$ in 1000 h-aged sample with prolonging aging time, in which the average value is about $\epsilon \sim 0.35\%$.

The OM image (Figure S3a) of the solid-solutionized alloy indicates that the alloy matrix consists of coarse ferritic grains with a size of 300–500 μm, where no second phase particles appear on grain boundaries. The precipitation of B2 nanoparticles in different heat-treated states was observed by SEM, as presented in Figure 1 and Figure S3. In the solid-solutionized state, the cuboidal B2 nanoparticles with a radius of $r \sim 30$ nm are uniformly distributed in the ferritic matrix (Figure 1a). Moreover, there also exist ultra-fine (< 5 nm) spherical nanoparticles, which might be caused by the secondary precipitation during water quenching [30]. After aging at 973 K, these cuboidal nanoparticles are regularized gradually with prolonging the aging time, and the ultra-fine nanoparticles disappear. In particular, the radius of these cuboidal B2 nanoprecipitates increases gradually from $r \sim 37$ nm for 0.5 h-aging to $r \sim 78$ nm for 100 h-aging (Figure 1b and c and Figure S3b–e). With further increasing the aging time, the particle size would increase more slowly from $r \sim 88$ nm for 200 h-aging
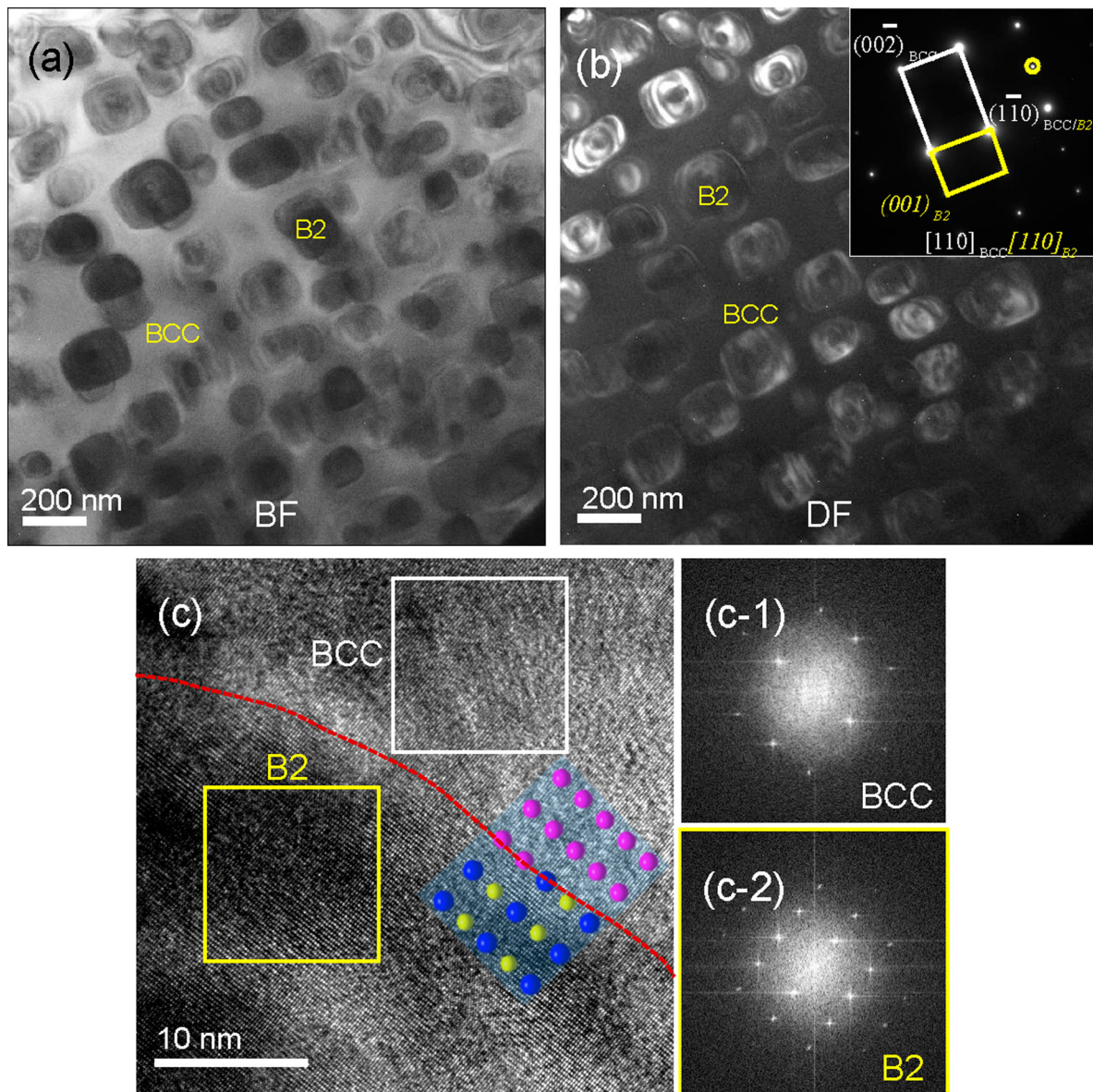

Figure 2. TEM characterization of the current alloy aged at 973 K for 48 h. The bright-field (BF) image (a) and the corresponding dark-field (DF) image (b) show that the cuboidal B2 nanoprecipitates are dispersed into the BCC matrix; HRTEM image and FFT patterns (c, c-1, c-2) exhibit that the B2 particle is coherent with the BCC matrix.

to $r \sim 114\,$nm for 500 h-aging, then to $r \sim 136\,$nm for 1000 h-aging, as seen in Figure 1(d–f). It is noted that no other second phases appear on the grain boundaries even after 1000 h-aging, as presented in the inset of Figure 1(f). In addition, the volume fraction of cuboidal B2 precipitates increases slightly from $f \sim 20.4\%$ in 0.5 h-aged state to $f \sim 24.8\%$ in 48 h-aged state, and then does not vary with the aging time. Coherent precipitates in ferritic alloys were generally coarsened by the agglomeration of particles during aging, leading to an almost-constant volume fraction [31]. To investigate the variation of B2 particles at a much higher temperature, the solid-solutionized alloy was further aged at 1073 K for up to 100 h, in which the B2 nanoparticles still maintain cuboidal, similar to that in 973 K-aged state. However, the B2 nanoparticles in 1073 K-aged state are coarsened, as evidenced by the particle size increasing from $r \sim 141\,$nm for 24 h-aging to $r \sim 158\,$nm for 48 h-aging, then to $r \sim 175\,$nm for 100 h-aging (Figure S4), which is much faster than that in 973 K-aged state.

The 48 h-aged alloy samples were further analysed by the TEM to verify the crystalline structure of precipitates, as shown in Figure 2. It is the cuboidal B2 nanoprecipitates embedded into the BCC matrix, as demonstrated by the selected area electron diffraction (SAED) pattern along the $[110]_{BCC}$ direction in both bright-field (BF) and dark-field (DF) images (Figure 2a and b). The high-resolution TEM (HRTEM) image and fast Fourier transform (FFT) patterns presented in Figure 2(c, c-1, c-2) indicate that the interface between B2 particle and BCC matrix is coherent, where the schematic crystalline

structures of BCC and B2 phases are also inserted in Figure 2(c). The elemental distribution in the 48 h-aged alloy was also analysed with the EDS equipped in DB-FIB, as shown in Figure 3. It is found that Ni and Al elements are enriched in B2 nanoparticles, and Fe, Cr, Mo, and W are mainly segregated in the BCC matrix.

Since the volume fraction of B2 nanoprecipitates remains almost unchanged with the aging time prolonging in the current alloy, the classic Ostwald ripening theory proposed by Philippe and Voorhees (i.e. the PV theory) could be applied to study the coarsening behaviour of B2 nanoparticles, which has been extensively used in multicomponent alloys [32,33]. Such a time-dependent coarsening process could be described with the following Equation (1):

$$r^3(t) - r^3(t_0) = k(t - t_0) \qquad (1)$$

where $r(t)$ is the mean radius of precipitates at the aging time t; $t_0 = 0\,$h represents the solid-solutionized state; and k is the coarsening rate constant. Figure 4(a) gives the variation of particle size r^3 of B2 nanoprecipitates with the aging time, which could be well fitted by the PV theory. Thus the coarsening rate constant is obtained as $k = 6.9 \times 10^{-28}$ m$^3 \cdot$s^{-1}. For comparison, we also plotted the variation of r^3 of particles with the aging time at 973 K in existing FBB8 and Ti-modified FBB8 alloys, from which the coarsening rate constants are 4.9×10^{-28} m$^3 \cdot$s^{-1} and 5.9×10^{-28} m$^3 \cdot$s^{-1}, respectively, comparable to that of the current alloy. The coarsening rate constant of coherent particles in BCC steels is much lower than that ($\sim 1.7 \times 10^{-26}$ m$^3 \cdot$s^{-1} at 873 K) of $Cr_{23}C_6$ carbides in Fe–9Cr–1Mo–0.2V–0.1C–0.08Nb–0.05N (wt. %, T91)
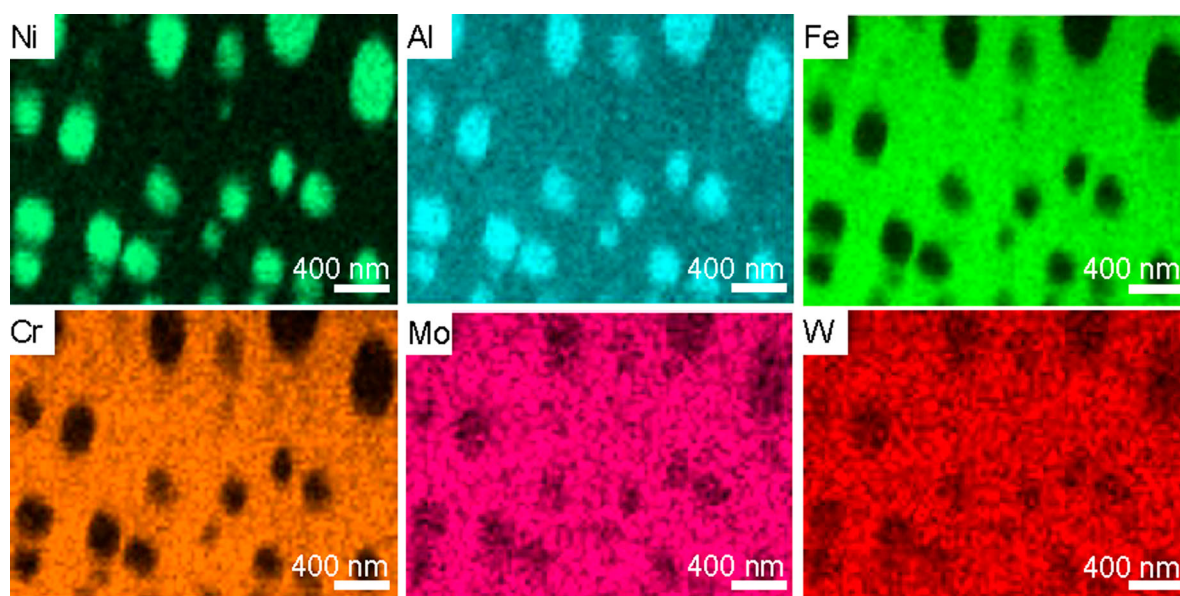

Figure 3. Elemental distribution of the 48 h-aged alloy mapped with EDS equipped in DB-FIB.
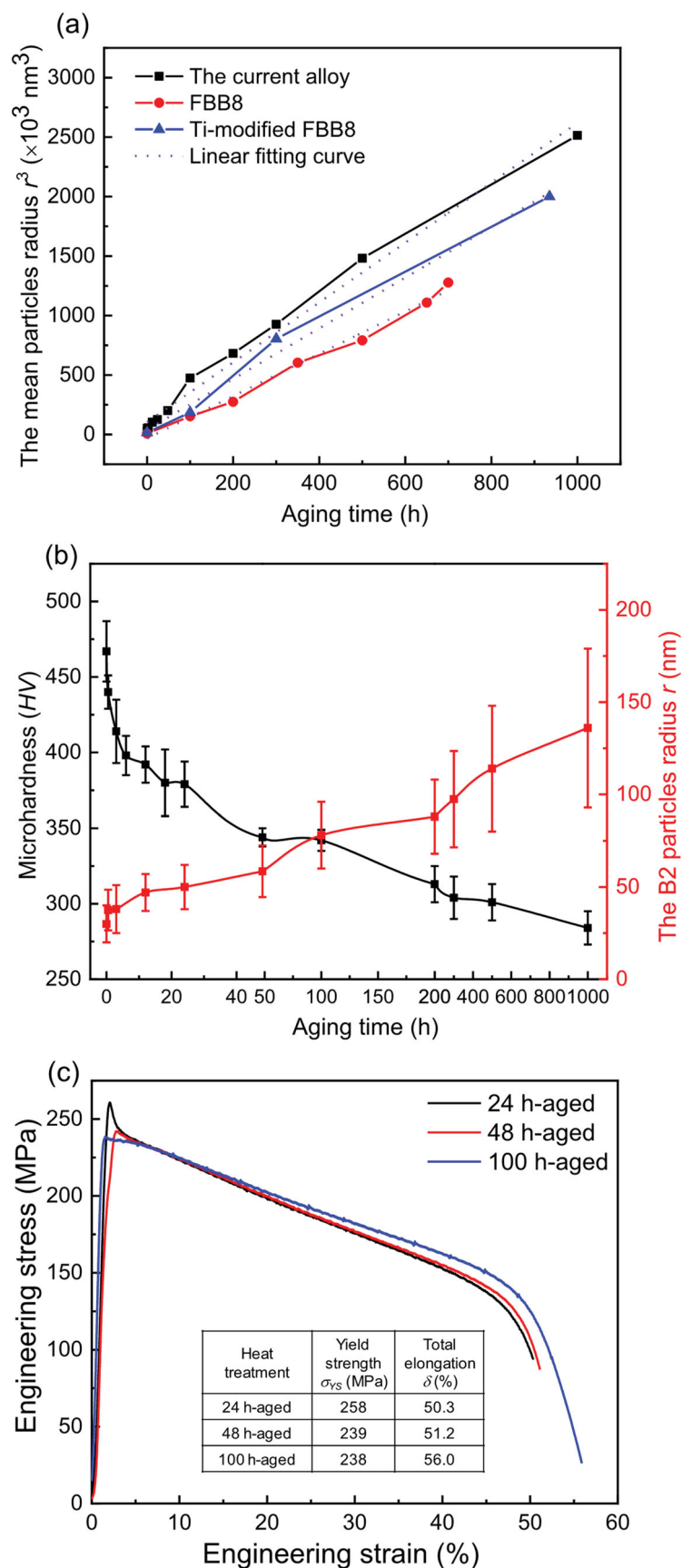
Figure 4. (a) Variation of the mean particle radius r^3 with the aging time at 973 K for the current alloy, FBB8, and Ti-modified FBB8, where the corresponding linear fitting curves are also shown; (b) variation tendency of the microhardness *HV* and B2 particle radius *r* in the current alloy with aging time at 973 K; (c) engineering tensile stress-strain curves at 973 K of the aged alloy for 24, 48, and 100 h.

steel [34], showing a much slower coarsening behaviour and a higher microstructural stability.

It is known that the equilibrium morphology of precipitates is strongly dependent on both the elastic strain energy and the interfacial energy at the precipitate/matrix interface, which could be described by the characteristic parameter, $L = \epsilon^2 C_{44} r/\sigma$, being proportional to the lattice misfit ϵ and the mean radius r of particles since the elastic strain energy is related to ϵ [35–37]. Then we calculated the L value of B2 nanoparticles in the current alloy, being $L = 0.16$–4.72, where the elastic constant of the BCC matrix is taken as $C_{44} = 116$ GPa [38], $\epsilon = 0.24$–0.67% and $r = 30$–136 nm for the current alloy, and the interfacial energy is $\sigma = 0.15$ J·m^{-2} [39]. Although the L value increases gradually from 0.16 after 0.5 h-aging to 4.72 after 1000 h-aging with prolonging aging time, it is still less than the critical value of $L^* = 5.6$, above which the particle morphology would change from cuboid to plate-like or needle-like shape [37]. Therefore, this moderate lattice misfit ($\epsilon = 0.24$–0.67%) contributes to the formation of cuboidal B2 nanoprecipitates in the current alloy.

Microhardness (HV) measurements were initially conducted to evaluate the age-hardening response of the current alloy. The variation of HV with the aging time at 973 K is presented in Figure 4(b), in which the tendency of the radius of the B2 particles is also shown. It is found that the HV decreases rapidly from $\sim 467\ HV$ in the solid-solutionized state to $\sim 419\ HV$ after 0.5 h-aging, which might result from the dissolution of ultra-fine spherical B2 nanoparticles into the BCC matrix since the particle size (60–70 nm) of cuboidal B2 nanoparticles in both states are comparable (Figure 2a and b). Then, it keeps almost constant till 24 h-aging, followed by a slight decrease to $\sim 344\ HV$ (48 h-aged), to $\sim 304\ HV$ (300 h-aged), and lastly to $\sim 284\ HV$ after 1000 h-aging. The slow decrease of HV in the late-period aging is ascribed to the relatively high thermal stability of B2 nanoparticles. Moreover, the precipitation of cuboidal B2 particles in the current alloy could achieve the maximum strengthening effect (see the details in Supplementary Material).

High-temperature tensile tests at 973 K of the aged alloy specimens for 24, 48, and 100 h were subsequently performed, and the engineering stress–strain curves are shown in Figure 4(c), from which the yield strength (σ_{YS}) and elongation to fracture (δ) are measured. It is found that the mechanical properties of these aged samples are comparable, with a yield strength of $\sigma_{YS} = 238$–258 MPa and a ductility of $\delta = 50$–56% at 973 K. Obviously, the σ_{YS} of this alloy is much higher than that ($\sigma_{YS} = 120$ MPa at 973 K) of FBB8 alloy containing spherical B2 precipitates (~ 53 nm) [10,13], and is slightly lower than that ($\sigma_{YS} = 280$ MPa at 973 K) of

Ti-modified FBB8 alloy containing cuboidal B2/L2$_1$ precipitates (~ 57 nm) [11,13]. It is mainly ascribed to the lattice misfit ϵ between BCC and B2/L2$_1$ phases, in which a larger ϵ would induce a stronger elastic strain field to hinder dislocation motion [40]. Indeed, it has been demonstrated that the dominant creep mechanism of FBB8 alloy at 973 K is the dislocation climb bypassing of B2 nanoprecipitates with repulsive elastic interaction strain field induced by the lattice misfit [24,40]. Thus the threshold strength (σ_{th}) for dislocations to bypass particles is strongly affected by the lattice misfit ϵ between BCC and B2 phases. Generally, the magnitude of threshold strength (σ_{th}) is about 0.4–0.5 times of the strength increment from the Orowan mechanism ($\Delta\sigma_{orowan}$) [24,40]. The threshold strength of the current alloy is then roughly estimated to be $\sigma_{th} = 148$–185 MPa with the Eq. (S1-c), in which $G = 57$ GPa at 973 K [41], $f = 24.8\%$ and $r = 78$ nm for the 100 h-aged alloy were taken. It is found that this value is much greater than that ($\sigma_{th} = 69$ MPa) of FBB8 alloy, and comparable to that ($\sigma_{th} = 172$ MPa) of Ti-modified FBB8 [13,24,42]. It is mainly ascribed to the relatively-large lattice misfit ($\epsilon = 0.24$–0.67% for the current alloy and $\epsilon = 0.7\%$ for Ti-modified FBB8 alloy) that generates a strong elastic strain field to impede the dislocation climbing, compared to the FBB8 alloy ($\epsilon = 0.06\%$) [10,11,42,43]. However, an excessive lattice misfit would reduce the threshold strength due to the fading coherency, as evidenced by the fact that the threshold strength of the FBB8 alloy modified by 4 wt. % Ti decreases down to $\sigma_{th} = 143$ MPa due to the $\epsilon \sim 1.3\%$ [30,42,44,45]. Therefore, a moderate lattice misfit ($\epsilon = 0.2$–0.7%) is necessary to both the formation of cuboidal B2 nanoprecipitates and the high microstructural stability at HTs, which finally contributes to the achievement of an optimal mechanical property.

Conclusion

In conclusion, we obtained a new Fe-based superalloy of Fe–10.9Cr–13.9Ni–6.4Al–2.2Mo–0.5W–0.04Zr–0.005B (wt. %) containing a special coherent microstructure of cuboidal B2-NiAl nanoparticles precipitated into BCC matrix. Even after long-term aging at 973 K for 1000 h, these B2 particles still keep cuboidal with a relatively low coarsening rate constant, as evidenced by the particle size being changed from $r \sim 60$ nm in solid-solutionized state to $r \sim 136$ nm in 1000 h-aged state. It is mainly ascribed to the moderate lattice misfit ($\epsilon = 0.24$–0.67%) between BCC and B2 phases. Moreover, it is the cuboidal B2 nanoprecipitation in the BCC matrix that renders the alloy with high microstructural stability

and high mechanical strength ($\sigma_{YS} = 238$–258 MPa) at 973 K.

Disclosure statement

No potential conflict of interest was reported by the author(s).

References

[1] Pesicka J, Kuzel R, Dronhofer A, et al. The evolution of dislocation density during heat treatment and creep of tempered martensite ferritic steels. Acta Mater. 2003;51:4847–4862.

[2] Kostka A, Tak KG, Hellmig RJ, et al. On the contribution of carbides and micrograin boundaries to the creep strength of tempered martensite ferritic steels. Acta Mater. 2007;55:539–550.

[3] Aghajani A, Somsen C, Eggeler G. On the effect of long-term creep on the microstructure of a 12% chromium tempered martensite ferritic steel. Acta Mater. 2009;57:5093–5106.

[4] Xu YT, Li W, Wang MJ, et al. Nano-sized MX carbonitrides contribute to the stability of mechanical properties of martensite ferritic steel in the later stages of long-term aging. Acta Mater. 2019;175:148–159.

[5] Niu B, Wang ZH, Wang Q, et al. Dual-phase synergetic precipitation in Nb/Ta/Zr co-modified Fe–Cr–Al–Mo alloy. Intermetallics. 2020;124:106848.

[6] Reed RC. The superalloys: fundamentals and applications. Cambridge: Cambridge University Press; 2008.

[7] Pollock TM, Argon AS. Creep resistance of CMSX-3 nickel base superalloy single crystals. Acta Metall Mater. 1992;40:1–30.

[8] Zhang JX, Harada H, Koizumi Y, et al. Dislocation motion in the early stages of high-temperature low-stress creep in a single-crystal superalloy with a small lattice misfit. J Mater Sci. 2010;45:523–532.

[9] Teng ZK, Ghosh G, Miller MK, et al. Neutron-diffraction study and modeling of the lattice parameters of a NiAl-precipitate-strengthened Fe-based alloy. Acta Mater. 2012;60:5362–5369.

[10] Teng ZK, Miller MK, Ghosh G, et al. Characterization of nanoscale NiAl-type precipitates in a ferritic steel by electron microscopy and atom probe tomography. Scripta Mater. 2010;63:61–64.

[11] Song G, Sun ZQ, Poplawsky JD, et al. Microstructural evolution of single Ni$_2$TiAl or hierarchical NiAl/Ni$_2$TiAl precipitates in Fe–Ni–Al–Cr–Ti ferritic alloys during thermal treatment for elevated-temperature applications. Acta Mater. 2017;127:1–16.

[12] Song G, Hong SJ, Lee JK, et al. Optimization of B2/L2$_1$ hierarchical precipitate structure to improve creep resistance of a ferritic Fe–Ni–Al–Cr–Ti superalloy via thermal treatments. Scripta Mater. 2019;161:18–22.

[13] Song G, Sun Z, Li L, et al. Ferritic alloys with extreme creep resistance via coherent hierarchical precipitates. Sci Rep. 2015;5:16327.

[14] Kohyama A, Hishinuma A, Gelles DS, et al. Low-activation ferritic and martensitic steels for fusion application. J Nucl Mater. 1996;233-277:138–147.

[15] Wang Q, Ma Y, Jiang BB, et al. A cuboidal B2 nanoprecipitation-enhanced body-centered-cubic alloy Al$_{0.7}$CoCrFe$_2$Ni with prominent tensile properties. Scripta Mater. 2016;120:85–89.

[16] Ma Y, Wang Q, Jiang BB, et al. Controlled formation of coherent cuboidal nanoprecipitates in body-centered cubic high-entropy alloys based on Al$_2$(Ni,Co,Fe,Cr)$_{14}$ compositions. Acta Mater 2018;147:213–225.

[17] Wang Q, Han JC, Liu YF, et al. Coherent precipitation and stability of cuboidal nanoparticles in body-centered-cubic Al$_{0.4}$Nb$_{0.5}$Ta$_{0.5}$TiZr$_{0.8}$ refractory high entropy alloy. Scripta Mater. 2021;190:40–45.

[18] Thompson M, Su C, Voorhees PW. The equilibrium shape of a misfitting precipitate. Acta Metall Mater. 1994;42(6):2107–2122.

[19] Yamamoto Y, Brady MP, Lu ZP, et al. Creep-resistant, Al$_2$O$_3$-forming austenitic stainless steels. Science. 2007; 316:433–436.

[20] Wang WR, Wang WL, Yeh JW. Phases, microstructure and mechanical properties of Al$_x$CoCrFeNi high-entropy alloys at elevated temperatures. J Alloys Compd. 2014;589:143–152.

[21] Chen RR, Qin G, Zheng HT, et al. Composition design of high entropy alloys using the valence electron concentration to balance strength and ductility. Acta Mater. 2018;144:129–137.

[22] Bhadeshia H, Honeycombe R. Steels-microstructure and properties. Oxford: Butterworth Heinemann; 2017.

[23] Calderon HA, Fine ME, Weertman JR. Coarsening and morphology of particles in Fe–Ni–Al–Mo ferritic alloys. Metall Trans A. 1987;19:1135–1146.

[24] Vo NQ, Liebscher CH, Rawlings MJS, et al. Creep properties and microstructure of a precipitation-strengthened ferritic Fe–Al–Ni–Cr alloy. Acta Mater. 2014;71:89–99.

[25] Briant CL, Banerji SK. Intergranular failure in steel: the role of grain boundary composition. Int Metal Rev. 1978;23:164–199.

[26] Baker I, Munroe PR. Improving intermetallic ductility and toughness. JOM. 1988;40:2.

[27] Schneider CA, Rasband WS, Eliceiri KW. NIH image to ImageJ: 25 years of image analysis. Nat Methods. 2012;9:671–675.

[28] Shackelford JF, Han YH. Kim S, et al. CRC Materials science and engineering handbook. Boca Raton (FL): CRC Press; 2016.

[29] Hosford WF. Mechanical behavior of materials. New York (NY): Cambridge University Press; 2005.

[30] Sun ZQ, Song G, Ilavsky J, et al. Duplex precipitates and their effects on the room-temperature fracture behavior of a NiAl-strengthened ferritic alloy. Mater Res Lett. 2015;3:128–134.

[31] Baik SI, Wang SY, Liaw PK, et al. Increasing the creep resistance of Fe–Ni–Al–Cr superalloys via Ti additions by optimizing the B2/L2$_1$ ratio in composite nanoprecipitates. Acta Mater. 2018;157:142–154.

[32] Philippe T, Voorhees PW. Ostwald ripening in multicomponent alloys. Acta Mater. 2013;61:4237–4244.

[33] Orthacker A, Haberfehlner A, Taendl J, et al. Diffusion-defining atomic-scale spinodal decomposition within nanoprecipitates. Nat Mater. 2018;17:1101–1107.

[34] Spigarelli S, Cerri E, Bianchi P, et al. Interpretation of creep behaviour of a 9Cr–Mo–Nb–V–N (T91) steel using threshold stress concept. Mater Sci Tech. 1999;15:1433.

[35] Voorhees PW, McFadden GB, Johnson WC. On the morphological development of second-phase particles in elastically-stressed solids. Acta Metall. 1992;40:2979–2992.

[36] Su CH, Voorhees PW. The dynamics of precipitate evolution in elastically stressed solids—II. Particle alignment. Acta Mater. 1996;44:2001–2006.

[37] Thompson M, Su C, Voorhees PW. The equilibrium shape of a misfitting precipitate. Acta Metall Mater. 1994;42(6):2107–2122.

[38] Wasilewski RJ. Elastic constants and young's modulus of NiAl. Trans Mct Soc AIME. 1966;236:455.

[39] Argon A. Strengthening mechanisms in crystal plasticity. Oxford: Oxford University Press; 2007.

[40] Zhao YX, Fang QH, Liu YW, et al. Creep behavior as dislocation climb over NiAl nanoprecipitates in ferritic alloy: The effects of interface stresses and temperature. Int J Plast. 2015;69:89–101.

[41] Ghosh G, Olson GB. The isotropic shear modulus of multicomponent Fe-base solid solutions. Acta Mater. 2002;50:2655–2675.

[42] Rawlings MJS, Liebscher CH, Asta M, et al. Effect of titanium additions upon microstructure and properties of precipitation-strengthened Fe–Ni–Al–Cr ferritic alloys. Acta Mater. 2017;128:103–112.

[43] Krug ME, Seidman DN, Dunand DC. Creep properties and precipitate evolution in Al-Li alloys microalloyed with Sc and Yb. Mater Sci Eng A. 2012;550:300–311.

[44] Song G, Sun ZQ, Clausen B, et al. Microstructural characteristics of a Ni$_2$TiAl-precipitate-strengthened ferritic alloy. J Alloys Compd. 2017;693:921–928.

[45] Polvani RS, Tzeng WS, Strutt PR. High temperature creep in a semicoherent NiAl-Ni$_2$AlTi alloy. Metall Trans A. 1973;7A:33–40.